Single-molecule analysis unveils the phosphorylation of FLS2 regulates its spatiotemporal dynamics and immunity

Yaning Cui[1,2,5], Hongping Qian[2,5], Jinhuan Yin[2], Changwen Xu[2], Pengyun Luo[2], Xi Zhang[2], Meng Yu[3], Bodan Su[4], Xiaojuan Li[2], Jinxing Lin[1,2*]

[1] Institute of Botany, Chinese Academy of Sciences, Beijing 10093, China
[2] College of Biological Sciences & Biotechnology, Beijing Forestry University, Beijing 100083, China
[3] College of Life Sciences, Hebei Agricultural University, Baoding, 071001, China
[4] School of Life Sciences, Tsinghua University, Beijing 100084, China
[5] These authors contributed equally

[*]Correspondence: Jinxing Lin (linjx@ibcas.ac.cn)

Summary

Phosphorylation of receptor-like kinases (RLKs) plays an important role in the regulation of pattern-triggered immunity (PTI). *Arabidopsis thaliana* FLAGELLIN-SENSITIVE2 (FLS2) is a typical RLK that can sense a conserved 22 amino acid sequence in the N-terminal region of flagellin (flg22) to initiate plant defense pathways. However, the mechanisms underlying the regulation of FLS2 phosphorylation activity at the plasma membrane in response to flg22 remain largely enigmatic. Here, by single-particle tracking, we demonstrated that Ser-938 phosphorylation site affected flg22-induced FLS2 spatiotemporal dynamics and dwell time. Furthermore, using Förster resonance energy transfer-fluorescence lifetime (FRET-FLIM) imaging microscopy coupled with protein proximity indexes (PPI), we revealed that the degree of co-localization of FLS2/FLS2^{S938D}-GFP with AtRem1.3-mCherry increased in response to flg22, whereas FLS2^{S938A}-GFP did not show significant changes, indicating that Ser-938 phosphorylation site facilitates efficient sorting of FLS2 into nanodomains. Importantly, we found that the Ser-938 phosphorylation of FLS2 significantly increased flg22-induced internalization and immune responses.

Taken together, these results illustrate that the phosphorylated site of FLS2 regulates the partitioning of FLS2 into functional membrane nanodomains to activate flg22-induced plant immunity.

Key words: single-molecule analysis; phosphorylation; spatiotemporal dynamics; membrane nanodomains; endocytosis; immunity;

Introduction

RLKs are structurally conservative proteins, containing an extracellular domain, single transmembrane region, and cytoplasmic kinase domain. The cytoplasmic kinase domains are composed of a protein kinase catalytic domain (PKC) and a juxtamembrane region, where PKC has phosphorylation sites, and phosphorylation modification on specific Ser and/or Thr residues is vital for PTI activation[1]. When pathogens invade, FLS2 releases BIK1 or homologs and associates with BAK1[2]; FLS2 kinase is then activated by phosphorylation. Multiple FLS2 phosphorylation sites have been identified, and Serine-938 was found to be important role for function of FLS2[3].

Membrane microdomains are highly dynamic structures that are rich in sterols and sphingolipids and regulate the behaviour of plasma membrane (PM) proteins[4-5]. Results from our study showed that flg22-induced plant immunity is affected in a sterol synthesis mutant, demonstrating that microdomains are associated with signal transduction in plant cells[6-8]. Phosphorylation serves as the endocytosis signal for several signaling receptors, and the phosphorylation of RLKs at the PM is crucial for endocytic functions[9]. Although Serine-938 phosphorylation site of FLS2 has been demonstrated, how it affects the immunity via its spatiotemporal dynamics remain poorly resolved.

Results and Discussion

The Ser-938 phosphorylation site changed spatiotemporal dynamics of flg22-induced FLS2 at the plasma membrane

Previous studies have indicated that phosphorylation of membrane proteins plays a critical role in fundamental cellular processes including PM dynamics[10-13]. The Ser-938 of FLS2 was previously identified as a functionally important site based on mass spectrometry experiments[3]. To determine the mechanisms underlying the regulation of immune response via phosphorylation of FLS2, we generated transgenic Arabidopsis plants expressing a C-terminal GFP fused to FLS2, S938A, or S938D under the control of the FLS2 native promoter in the fls2 mutant background (Figure S1A). Using VA-TIRFM combined with single-particle tracking (Figure 1A and 1B), we next investigated the diffusion dynamics of FLS2 phosphorylated and non-phosphorylated mutants following the methods reported previously[14]. When seedlings were treated with flg22, results showed that individual $FLS2^{S938D}$-GFP spots had longer motion trajectories, whereas $FLS2^{S938A}$-GFP spots were limited to much shorter motion tracks (Figure 1C). The results demonstrate that the diffusion coefficients and motion ranges of FLS2/$FLS2^{S938D}$-GFP changed significantly after flg22 treatment, whereas $FLS2^{S938A}$-GFP was not no significantly differences (Figure 1D and 1E). A similar result was observed using Uniform Manifold Approximation and Projection (UMAP) technology[15] and fluorescence recovery after photobleaching (FRAP) [16] (Figure 1F, 1G and S1B), supporting the idea that S938 phosphorylation site is essential for flg22-induced lateral diffusion of FLS2 at the PM.

Using VA-TIRFM, we also analyzed dwell time of FLS2 particles under different phosphorylation states. Our results showed that the flg22 treatment significantly shortened the fluorescence trajectory of FLS2 molecules compared with the control (Figure 1H and S1C), suggesting that Ser-938 phosphorylation site changes flg22-induced dwell times of FLS2 at the PM. Subsequently, we performed real-time dynamic analysis by Kymograph technique to obtain spatiotemporal information from frame-by-frame tracking[17].

We found that compared with FLS2-GFP and FLS2^{S938D}-GFP, the fluorescence fluctuation of FLS2^{S938A}-GFP under the condition of flg22 was nearly linear and exhibited a decreased fluorescence retention time (Figure S1D). To further confirm this possibility, we quantified FLS2 dwell times by fitting the exponential function (Figure 1I and S1E). The dwell times of FLS2^{S938D}-GFP after flg22 treatment were significantly shorter than those in the control seedlings, and similar to those of the FLS2-GFP. In FLS2^{S938A}-GFP plants, the dwell times appeared to slightly decrease in response to flg22 treatment, but this change was not significant. This is supported by the finding of Zhang et al. that the phosphorylation of NRT1.1 affects its dynamics and dwell time [18]. These results suggest that Ser-938 phosphorylation site affects the spatiotemporal dynamics of flg22-induced FLS2.

Ser-938 phosphorylation enhances recruitment of FLS2/BAK1 hetero-oligomerization into nanodomains

Proteins rarely act alone, and generally form multimers and potentiate downstream signaling[19]. Previously, we demonstrated that inactive FLS2 mostly exists as monomers, and that flg22 treatment induced FLS2 and BAK1 to form a hetero-dimer, suggesting that flg22 can act as a ligand-like factor to promote hetero-dimerization at PM[6]. Therefore, we wanted to monitor whether the FLS2/BAK1 heterooligomerization formation is phosphorylation-dependent. Tesseler technology, FRET-FLIM analysis, and smPPI revealed that Ser-938 phosphorylation states did not affect the hetero-oligomerization of FLS2/BAK1 (Figure 2A-C and S2), indicating that FLS2/BAK1 hetero-dimerization is independent of phosphorylation and that these two events occurred sequentially.

Membrane nanodomains serve as platforms for regulation of proteins dynamic and cellular signaling[20-22]. Several studies have revealed that some PM proteins can move inside and outside the membrane nanodomains to convey signals in response to developmental cues and environmental stimuli[13].

For example, treatment with the secreted peptide RAPID ALKALINIZATION FACTOR (RALF1 and RALF23) increased the amount of FERONIA (FER) in membrane nanodomains[24], whereas flg22-activated BSK1 moved from the membrane nanodomains to the non-membrane nanodomains[25]. Previous investigation showed that flg22 induces translocation of FLS2 from AtFlot1-negative to AtFlot1-positive nanodomains in the plasma membrane[6], so whether the phosphorylation state of FLS2 was associated with the distribution of membrane nanodomains. To test this hypothesis, we assessed the interaction between FLS2/FLS2^{S938D}/FLS2^{S938A} and AtRem1.3, the marker of sterol-rich rafts in the *Arabidopsis* PM. Using SPT, FRET–FLIM and Pearson correlation, it was found that FLS2-GFP/FLS2^{S938D}-GFP and AtRem1.3-mCherry exhibited higher correlation coefficients under flg22 treatment compared with the control (Figure 2D-2F). Notably, flg22 treatment did not increase the colocalization levels of FLS2^{S938A}-GFP and AtRem1.3, indicating that phosphorylation is required (Figure 2G-2I). Based on these results, we speculate that the phosphorylated FLS2 can aggregate into membrane nanodomains, which might provide an efficient way to mount the immune response.

Ser-938 phosphorylation is required to maintain FLS2 protein homeostasis via flg22-induced endocytosis

The endocytosis of PM proteins plays a key role in regulating signal transduction between cells and their environmental stimulation[26, 27]. Strikingly, mutation of Thr 867, a potential phosphorylation site of FLS2, leads to impaired flg22-induced endocytosis, suggesting that phosphorylation plays an important role in FLS2 endocytosis[28]. As described above, FLS2 phosphomimetic mutants showed a shorter dwell time (Figure 1 H and 1I), therefore, we speculate that the short of FLS2 dwell time is most likely related to endocytosis. Results found that FLS2/FLS2^{S938D}/FLS2^{S938A}-GFP all clearly accumulated in BFA compartments labeled with FM4-64, indicating that

different Ser-938 phosphorylation states of FLS2 can still undergo BFA-dependent constitutive endocytosis (Figure 3A, S3A).

Next, we wanted to understand whether Ser-938 affects the flg22-induced internalization of FLS2. Results showed that FLS2 exhibited more endocytic vesicles under flg22 treatment, which is consistent with the findings of previous studies[29-30]. Using CLSM, Fluorescence Correlation Spectroscopy (FCS) and Western blotting, we found that the endocytic vesicles of $FLS2^{S938D}$ increased significantly after flg22 treatment (Figure 3B-3E), however, there was little change in $FLS2^{S938A}$ in the absence or presence of the ligand (Figure S3C-G), implying the important role of FLS2 Ser-938 phosphorylation in flg22-induced internalization. Our results provided strong evidence that the phosphorylation of Ser-938 facilitates rapid internalization of FLS2, and this may regulate its FLS2 capacity for immune responses.

Ser-938 Phosphorylation affects FLS2-mediated responses

Plant innate immunity plays a vital role in inducing host defense against pathogen infections[31]. For instance, upon perception of the peptide Pep1 signal, a damage-associated molecular pattern can trigger the accumulation of defense hormones, induction of expression of defense genes, and inhibition of seedling growth[32]. After flg22 treatment, a series of immune responses, including activation of a calcium burst, mitogen-activated protein kinases (MAPKs), induction of immune-responsive genes and callose deposition[33-36], were induced in FLS2 and $FLS2^{S938D}$ plants, however, these immune response was limited in $FLS2^{S938A}$ (Figure 4A-D and S4A-B), indicating that the ability to phosphorylate Ser-938 is key for FLS2-mediated PTI responses. Most importantly, we found that the application of flg22 significantly inhibited growth of hypocotyl in the FLS-GFP and $FLS2^{S938D}$-GFP (Figure 4E-F and Figure S4C). This result supported the model of a trade-off between FLS2-mediated immunity and development[37-38].

In summary, our study of FLS2 phosphorylation reveals a novel and unexpected role in the regulation of PAMP-triggered plant immunity by regulating FLS2 the spatiotemporal dynamics at the PM (Figure 4 G and H). After flg22 treantment, activated FLS2 sequentially undergoes hetero-oligomerization and phosphorylation. More importantly, the Ser-938 phosphorylation site of FLS2 promotes FLS2 recruitment into nanodomains and endocytosis. These results provided new insights into the key mechanism of phosphorylation-regulated dynamics and plant immunity, which provides a reference for future studies on signal transduction of complex nanostructures in living cells.

Acknowledgments

This work was supported by the National Natural Science Foundation of China (32030010, 91954202, 32000483), National Key Research and Development Program of China (2022YFF0712500).

Author contributions

J.L., Y.C., and X.L. designed the research; Y.C., H.Q., and J.Y. performed the research; C.X., P.L.,and M.Y. contributed new reagents/analytic tools; X.Z., H.Q., and B.S. analyzed the data; and Y.C. and J.L. wrote the paper.

Declaration of interests

The authors declare no competing interests.

STAR Methods

Plant Materials and Construction

Mutants and transgenic lines used in all experiments were in the *Arabadopsis thaliana* Colombia-0 (Col-0) background. To generate the transgenic plants, specific constructs were PCR-amplified and cloned into the vector pCAMBIA2300. Plasmids were introduced into the mutant plants by *Agrobacterium*-mediated transformation. Dual-color lines expressing

FLS2^{S938A}-GFP and FLS2^{S938D}-GFP with REM1.3-mCherry were generated by hybridization.

Drug Treatments

All chemicals were obtained from Sigma-Aldrich, and dissolved in 100% DMSO to yield stock solutions at the following concentrations: BFA (50 mM in DMSO, 50 µM in working solution), CHX (50 mM in DMSO, 50 µM in working solution), and FM4-64 (5 mM in DMSO, 5 µM in working solution). The flg22 of flagellin peptides was synthesized by Shanghai GL Biochem Company, and was used in a concentration of 10 µM in double-distilled H2O. *Arabidopsis* seedlings were treated in 1/2 MS growth liquid medium with added hormone or drug.

Quantitative Reverse-transcription PCR

Total RNA was extracted using the Plant Kit (Tiangen), and then reverse transcribed into cDNA with FastQuant RT Kit (Tiangen). Next, qPCR was performed using TiangenSurperRealPreMix Plus (SYBR Geen). The primers used were as follows: WRKY33 (At At2g38470) 5′-GAAACAAATGGTGGGAATGG-3′ and 5′-TGTCGTGTGATGCTCTCTCC-3′; CYP81 (At At2g23190) 5′-AAATGGAGAGAGCAACACAATG-3′ and 5′-ATCGCCCATTCCAATGTTAC-3′; FRK1 (At At2g19190) 5′-TATATGGACACCGCGTATAGTG-3′and 5′-ATAAAACTTTGCGTTAGGGTCG-3′.

Aniline Blue Staining

To detect callose deposition, aniline blue staining was performed as described. *Arabidopsis thaliana* leaves were completely de-colored by the destaining solution (3 mL ethyl alcohol and 1 ml glacial acetic acid), rinsed in water and 50% ethanol, and then stained in 150 mM KH_2PO_4 (pH 9.5) plus 0.01% aniline blue for 2 h. Samples were mounted in 25% glycerol, and then observed under

a microscope that was equipped with a Leica DM2500 UV lamp.

Confocal Laser Scanning Microscopy and Image Analysis

Confocal microscopy was done with a TCS SP5 Confocal Microscope fitted with a 63X water-immersion objective. GFP and FM4-64 were assayed using 488-nm and 514-nm wavelengths (multitrack mode).The fluorescence emissions were respectively detected with spectral detector set LP 560–640 (FM4-64) and BP 520–555 (GFP). Image analysis was performed with Leica TCS SP5 software and quantified using the ImageJ software bundle (NIH).

VA-TIRFM and Single-Particle Fluorescence Image Analysis

The dynamics of FLS2 phosphomimetic and nonphosphorylatable mutants were recorded using VA-TIRFM. This was done using an inverted microscope (IX-71, Olympus) equipped with a total internal reflective fluorescence illuminator (model no. IX2-RFAEVA-2; Olympus) and a 1003 oil-immersion objective (numerical aperture = 1.45). To track GFP-labeled proteins at the PM, living leaf epidermal cells of 6-day-old seedlings were observed under VA-TIRFM. To visualize GFP or mCherry fluorescent proteins, appropriate corresponding laser excitation (473-nm or 561-nm) was used and emission fluorescence was obtained with filters (BA510IF for GFP; HQ525/50 for mCherry). A digital EMCCD camera (Andor Technology, ANDOR iXon DV8897D-CS0-VP, Belfast, UK) was used to acquire the fluorescent signals, which were stored directly on computers and then analyzed with Image J software. Images of single particles were acquired with 100-ms exposure time.

Analysis of Root Growth

Arabidopsis seedlings were treated with different conditions, and imaging was performed by scanning the root systems at 500 dpi (Canon EOS 600D). ImageJ was used to analyze the root growth parameters. Three biological replicates were performed.

FCS

FCS was performed in point-scanning mode on a Leica TCS SP5 FCS microscope equipped with a 488-nm argon laser, an Avalanche photodiode, and an in-house coupled correlator. After acquiring images on the PM of a cell in transmitted light mode, the diffusion of protein molecules into and out of the focal volume transformed the local concentration of fluorophores, leading to spontaneous fluctuation in the fluorescence intensity. Finally, the protein density was calculated on the basis of the protocol described previously.

FRET-FLIM

FRET-FLIM analysis was performed using an inverted Olympus FV1200 microscope equipped with a Picoquant picoHarp300 controller. The excitation at 488 nm was implemented by a picosecond pulsed diode laser at a reduplication rate of 40 MHz, by way of a water immersion objective (603, numerical aperture [NA] 1.2). The emitted light passed through a 520/35 nm bandpass filter and was detected by an MPD SPAD detector. Data were collected and performed using the SymphoTime 64 software (PicoQuant).

Western Blot

Total proteins were extracted from 10-day-old seedlings of the acidic phosphomimic mutants FLS2^{S938A}-GFP and FLS2^{S938D}-GFP and transgenic FLS2-GFP lines under different conditions. Proteins were extracted using buffer E [includes 1.5125 g Tris-HCl (pH 8.8), 1.2409 g $Na_2S_2O_5$, 11.1 ml glycerine, 1 g SDS, and 5 mM DTT]. The proteins in PM fractions were obtained using the Invent Minute kit. Proteins were separated by 10% SDS-polyacrylamide gel and transferred to a nitrocellulose membrane. The membrane was blotted with anti-GFP antibody (Sigma-Aldrich) at a 1:4000 dilution.

References

1. Yu, X., Xie, Y., Luo, D., Liu, H., de Oliveira, M. V. V., Qi, P., Kim, S. I., Ortiz-Morea, F. A., Liu, J., Chen, Y., et al. (2023). A phospho-switch constrains BTL2-mediated phytocytokine signaling in plant immunity. *Cell* **186**, 2329–2344.e20. 10.1016/j.cell.2023.04.027.
2. Schulze, S., Yu, L., Hua, C., Zhang, L., Kolb, D., Weber, H., Ehinger, A., Saile, S. C., Stahl, M., Franz-Wachtel, M., et al. (2022). The Arabidopsis TIR-NBS-LRR protein CSA1 guards BAK1-BIR3 homeostasis and mediates convergence of pattern- and effector-induced immune responses. *Cell Host Microbe* **30**, 1717–1731.e6. 10.1016/j.chom.2022.11.001.
3. Cao, Y., Aceti, D. J., Sabat, G., Song, J., Makino, S., Fox, B. G., and Bent, A. F. (2013). Mutations in FLS2 Ser-938 dissect signaling activation in FLS2-mediated Arabidopsis immunity. *PLOS Pathog* **9**, e1003313. 10.1371/journal.ppat.1003313.
4. Boutté, Y., and Jaillais, Y. (2020). Metabolic cellular communications: feedback mechanisms between membrane lipid homeostasis and Plant Development. Dev. Cell 54, 171–182. 10.1016/j.devcel.2020.05.005.
5. Wang L, Xue Y, Xing J, Song K, Lin J. (2018). Exploring the Spatiotemporal Organization of Membrane Proteins in Living Plant Cells. *Annu Rev Plant Biol*. **69**, 525-551. doi: 10.1146/annurev-arplant-042817-040233.
6. Cui, Y., Li, X., Yu, M., Li, R., Fan, L., Zhu, Y., and Lin, J. (2018). Sterols regulate endocytic pathways during flg22-induced defense responses in Arabidopsis. *Development* **145**, dev165688. 10.1242/dev.165688.
7. Wang Q, Zhao Y, Luo W, Li R, He Q, Fang X, Michele RD, Ast C, von Wirén N, Lin J. (2013). Single-particle analysis reveals shutoff control of the Arabidopsis ammonium transporter AMT1;3 by clustering and internalization. *Proc Natl Acad Sci U S A*. **110**:13204-9. doi: 10.1073/pnas.1301160110.
8. Eichel K, Jullié D, von Zastrow M. (2016).β-Arrestin drives MAP kinase signalling from clathrin-coated structures after GPCR dissociation. *Nat Cell Biol*. **18**:303-10. doi: 10.1038/ncb3307.
9. Palladino END, Bernas T, Green CD, Weigel C, Singh SK, Senkal CE, Martello A, Kennelly JP, Bieberich E, Tontonoz P, Ford DA, Milstien S, Eden ER, Spiegel S. (2022). Sphingosine kinases regulate ER contacts with late endocytic organelles and cholesterol trafficking. *Proc Natl Acad Sci U S A*. **119**:e2204396119. doi: 10.1073/pnas.2204396119.
10. Offringa, R., and Huang, F. (2013). Phosphorylation-dependent trafficking of plasma membrane proteins in animal and plant cells. *J Integr Plant Biol* **55**, 789–808. 10.1111/jipb.12096.
11. Van Itallie, C. M., and Anderson, J. M. (2018). Phosphorylation of tight junction transmembrane proteins: many sites, much to do. *Tissue barriers* **6**, e1382671. 10.1080/21688370.2017.1382671.
12. Monje-Galvan, V., Warburton, L., and Klauda, J. B. (2019). Setting up all-atom molecular dynamics simulations to study the interactions of peripheral membrane proteins with model lipid bilayers. *Methods Mol. Biol* **1949**, 325–339. 10.1007/978-1-4939-9136-5_22.
13. Trotta, A., Bajwa, A. A., Mancini, I., Paakkarinen, V., Pribil, M., and Aro, E. M. (2019). The role of phosphorylation dynamics of CURVATURE THYLAKOID 1B in plant thylakoid membranes. *Plant Physiol* **181**, 1615–1631. 10.1104/pp.19.00942.
14. Geng, X., Ge, B., Liu, Y., Wang, X., Dong, K., Zhang, Y., Chen, Y., and Lu, C. (2022). Genome-wide identification and functional analysis of silicon transporter family genes in

moso bamboo (Phyllostachys edulis). *Int. J. Biol. Macromol* **223**, 1705–1719. 10.1016/j.ijbiomac.2022.10.099.

15. Dorrity, M. W., Saunders, L. M., Queitsch, C., Fields, S., and Trapnell, C. (2020). Dimensionality reduction by UMAP to visualize physical and genetic interactions. *Nat. Commun* **11**, 1537. 10.1038/s41467-020-15351-4.
16. Greig, J., and Bulgakova, N. A. (2021). Fluorescence recovery after photobleaching to study the dynamics of membrane-bound proteins in vivo using the Drosophila embryo. *Methods Mol. Biol* **2179**, 145–159. 10.1007/978-1-0716-0779-4_13.
17. Zhou R, Liu H, Ju T, Dixit R. (2020).Quantifying the polymerization dynamics of plant cortical microtubules using kymograph analysis. *Methods Cell Biol* **160**:281-293. doi: 10.1016/bs.mcb.2020.04.006.
18. Zhang, X., Cui, Y., Yu, M., Su, B., Gong, W., Baluška, F., Komis, G., Šamaj, J., Shan, X., and Lin, J. (2019). Phosphorylation-mediated dynamics of nitrate transceptor NRT1.1 regulate auxin flux and nitrate signaling in lateral root growth. *Plant Physiol* **181**, 480–498. 10.1104/pp.19.00346.
19. Li, M., Ong, C. Y., Langouët-Astrié, C. J., Tan, L., Verma, A., Yang, Y., Zhang, X., Shah, D. K., Schmidt, E. P., and Xu, D. (2022). Heparan sulfate-dependent RAGE oligomerization is indispensable for pathophysiological functions of RAGE. *eLife* **11**, e71403. 10.7554/eLife.71403.
20. Sato, K. I., and Tokmakov, A. A. (2019). Membrane microdomains as platform to study membrane-associated events during oogenesis, meiotic maturation, and fertilization in xenopus laevis. *Methods Mol. Biol* **1920**, 59–73. 10.1007/978-1-4939-9009-2_5.
21. Ozolina, N.V., Kapustina, I.S., Gurina, V.V., Bobkova, V.A., and Nurminsky, V.N. (2021). Role of plasmalemma microdomains (Rafts) in protection of the plant cell under osmotic stress. *J. Membr. Biol* **254**, 429-439. 10.1007/s00232-021-00194-x.
22. Xu, C., Abbas, S., Qian, H., Yu, M., Zhang, X., Li, X., Cui, Y., and Lin, J. (2022). Environmental cues contribute to dynamic plasma membrane organization of nanodomains containing Flotillin-1 and hypersensitive induced reaction-1 proteins in Arabidopsis thaliana. *Front. Plant Sci* **13**, 897594. 10.3389/fpls.2022.897594.
23. Boutté, Y., and Moreau, P. (2014). Plasma membrane partitioning: from macro-domains to new views on plasmodesmata. *Front. Plant Sci.* **5**, 128. 10.3389/fpls.2014.00128.
24. Yu, M., Cui, Y., Zhang, X., Li, R., and Lin, J. (2020). Organization and dynamics of functional plant membrane microdomains. *Cell. Mol. Life Sci* **77**, 275–287. 10.1007/s00018-019-03270-7.
25. Su, B., Zhang, X., Li, L., Abbas, S., Yu, M., Cui, Y., Baluška, F., Hwang, I., Shan, X., and Lin, J. (2021). Dynamic spatial reorganization of BSK1 complexes in the plasma membrane underpins signal-specific activation for growth and immunity. *Mol Plant* **14**, 588–603. 10.1016/j.molp.2021.01.019.
26. Zhao, Z., Li, M., Zhang, H., Yu, Y., and Ma, L., et al. (2022). Comparative proteomic analysis of PM proteins in rice leaves reveals a vesicle trafficking network in plant immunity that is provoked by blast fungi. *Frontiers in Plant Science* **13:**853195.
27. Hilgemann, D. W., Dai, G., Collins, A., Lariccia, V., Magi, S., Deisl, C., and Fine, M. (2018). Lipid signaling to membrane proteins: from second messengers to membrane domains and adapter-free endocytosis. *J. Gen. Physiol* **150**, 211–224. 10.1085/jgp.201711875.

28. Robatzek, S., Chinchilla, D., and Boller, T. (2006). Ligand-induced endocytosis of the pattern recognition receptor FLS2 in Arabidopsis. *Genes Dev* **20**, 537–542. 10.1101/gad.366506.
29. Leslie, M. E., and Heese, A. (2017). Quantitative analysis of ligand-induced endocytosis of FLAGELLIN-SENSING 2 using automated image segmentation. *Methods Mol Biol* **1578**, 39–54. 10.1007/978-1-4939-6859-6_4.
30. Loiseau, J., and Robatzek, S. (2017). Detection and analyses of endocytosis of plant receptor kinases. *Methods Mol. Biol* **1621**, 177–189. 10.1007/978-1-4939-7063-6_17.
31. Joshi, R., Paul, M., Kumar, A., and Pandey, D. (2019). Role of calreticulin in biotic and abiotic stress signalling and tolerance mechanisms in plants. *Gene* **714**, 144004. 10.1016/j.gene.2019.144004.
32. Liu, Z., Wu, Y., Yang, F., Zhang, Y., Chen, S., Xie, Q., Tian, X., and Zhou, J. M. (2013). BIK1 interacts with PEPRs to mediate ethylene-induced immunity. *Proc. Natl. Acad. Sci* **110**, 6205–6210. 10.1073/pnas.1215543110.
33. Chen, Y., Cao, C., Guo, Z., Zhang, Q., and Li, S., et al. (2020). Herbivore exposure alters ion fluxes and improves salt tolerance in a desert shrub. *Plant Cell Environ* **43**, 400-419. 10.1111/pce.13662
34. Chi, Y., Wang, C., Wang, M., Wan, D., and Huang, F., et al. (2021). Flg22-induced Ca2+ increases undergo desensitization and resensitization. *Plant Cell Environ* **44**, 3793-3805. 10.1111/pce.14186
35. Zhang, M., Su, J., Zhang, Y., Xu, J., and Zhang, S. (2018). Conveying endogenous and exogenous signals: MAPK cascades in plant growth and defense. *Curr Opin Plant Biol* **45**, 1-10. 10.1016/j.pbi.2018.04.012
36. Arnaud D, Deeks MJ, Smirnoff N. (2023). RBOHF activates stomatal immunity by modulating both reactive oxygen species and apoplastic pH dynamics in Arabidopsis. *Plant J*. 10.1111/tpj.16380
37. Zou, Y., Wang, S., Zhou, Y., Bai, J., Huang, G., Liu, X., Zhang, Y., Tang, D., and Lu, D. (2018). Transcriptional regulation of the immune receptor FLS2 controls the ontogeny of plant innate immunity. *Plant Cell* **30**, 2779–2794. 10.1105/tpc.18.00297.
38. Ngou, B. P. M., Jones, J. D. G., and Ding, P. (2022). Plant immune networks. *Trends Plant Sci* **27**, 255–273. 10.1016/j.tplants.2021.08.012.

Figures and Figure legends

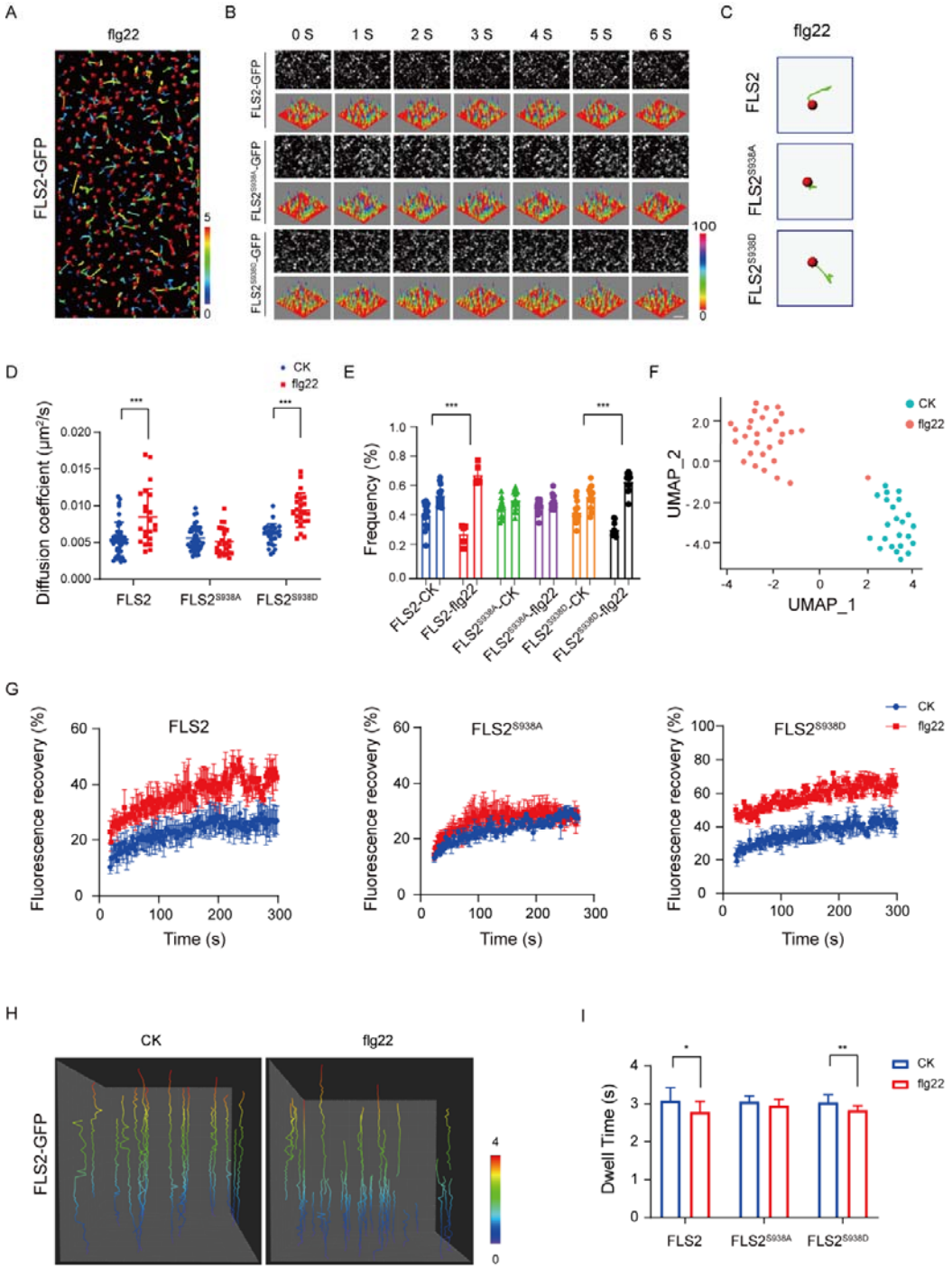

Figure 1. Effects of Ser-938 phosphorylation on the spatiotemporal

dynamics of FLS2 at the plasma membrane.

(A) VA-TIRFM image of a hypocotyl cell expressing FLS2 was analyzed. The red balls indicate the positions of the identified points that appeared. Trajectories represent the track length of the identified points. (**B**) Time-lapse images of FLS, $FLS2^{S938A}$, and $FLS2^{S938D}$. Bar = 200 μm. The changes of fluorescence intensity among different 3D luminance plots. (**C**) The trajectories of representative individual FLS2, $FLS2^{S938A}$ and $FLS2^{S938D}$ under flg22 processing. (**D**) Diffusion coefficients of FLS, $FLS2^{S938A}$ and $FLS2^{S938D}$ under different environments. (**E**) Frequency of long- and short-range motions for FLS, $FLS2^{S938A}$ and $FLS2^{S938D}$ under different environments. (**F**) UMAP visualization of $FLS2^{S938D}$ samples in the same conditions. Dots represent individual images and are colored according to the reaction conditions. (**G**) Fluorescence recovery curves of the photobleached areas with or without flg22 treatment. (**H**) The single molecule trajectories of FLS2 analyzed by Imaris could be faithfully tracked for 10 s under control and flg22 treatments. (**I**) Dwell times were analyzed for FLS2, $FLS2^{S938A}$ and $FLS2^{S938D}$ in the presence of the control and flg22 treatment.

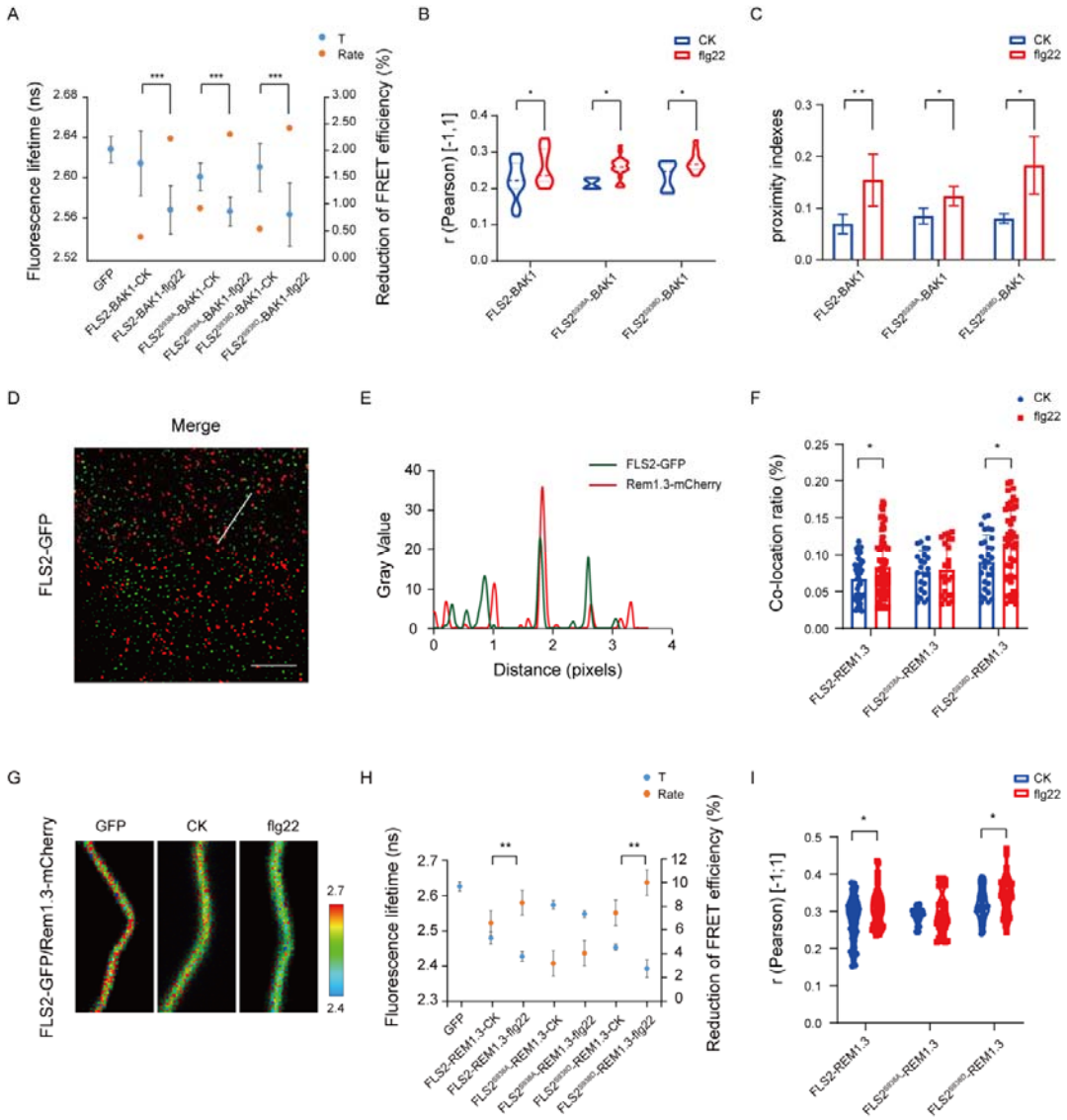

Figure 2. Different Ser-938 phosphorylation states of FLS2 affects its partitioning into membrane nanodomains.

(A) Average fluorescence lifetime (t) and the FRET efficiency were analyzed of FLS2, FLS2^{S938A} or FLS2^{S938D} and BAK1. (**B**) Pearson correlation coefficient values of co-localization between FLS2, FLS2^{S938A} or FLS2^{S938D} and BAK1 upon stimulation with CK or flg22. (**C**) Mean protein proximity indexes showing FLS2, FLS2^{S938A} or FLS2^{S938D} and BAK1 degree of proximity. (**D**) TIRM-SIM images of the leaf epidermal cells co-expressing FLS2 and AtRem1.3. The white line represents the fluorescence signals. Bar = 5 μm. (**E**)

FLS2 and AtRem1.3 fluorescence signals as shown in A. (**F**) The histogram shows the co-localization ratio of FLS2, $FLS2^{S938D}$ or $FLS2^{S938A}$ and AtRem1.3-mCherry. (**G**) Intensity and lifetime maps of the cells co-expressing FLS2 and AtRem1.3 as measured by FLIM-FRET. (**H**) The fluorescence mean lifetime (T) and the corrected fluorescence resonance efficiency (Rate) of FLS2, $FLS2^{S938D}$ or $FLS2^{S938A}$ with co-expressed AtRem1.3. (**I**) Quantification of co-localization between FLS2, $FLS2^{S938A}$ or $FLS2^{S938D}$ and AtRem1.3 with and without stimulation with ligands.

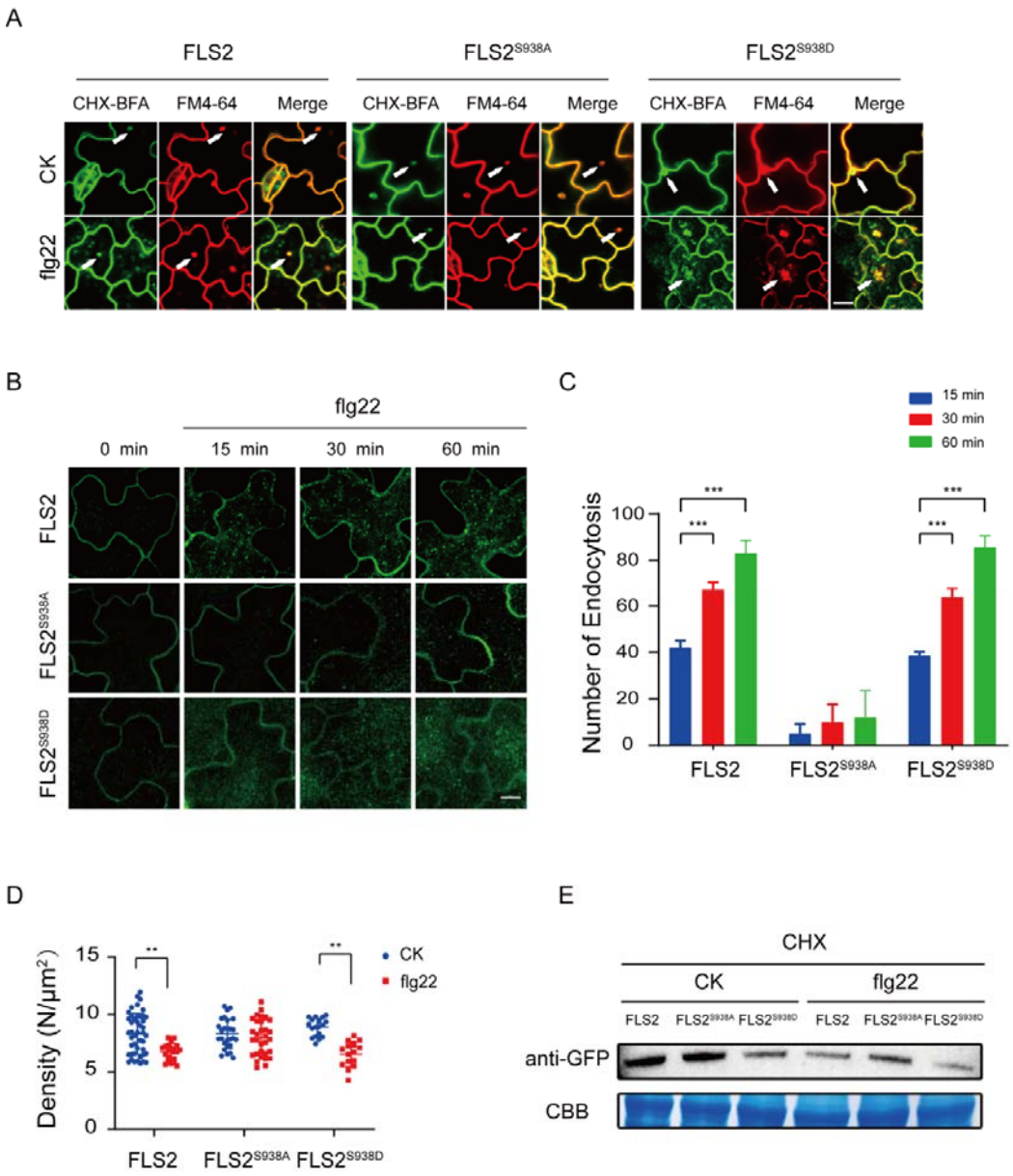

Figure 3. Ser-938 phosphorylation site affects flg22-induced endocytosis.

(A) Images of FLS2, FLS2^{S938D} and FLS2^{S938A} in leaf epidermal cells of *Arabidopsis thaliana*. Transgenic seedlings were pretreated with CHX for 30 min, then treated with CHX + BFA for 60 min or CHX + BFA + FM4-64 for 30 min, followed by 10 μM flg22 treatment for a total of 30 minutes. White arrows indicate BFA bodies. Bar=3μm. (**B**) Images of FLS2, FLS2^{S938A} and FLS2^{S938D} in cells treated with flg22 for 15, 30, and 60 min. Bar=3μm. (**C**) Number

analysis of FLS2, $FLS2^{S938A}$ and $FLS2^{S938D}$ endocytosis in cells treated with flg22 treatment over time. (**D**) The signal density of FLS2, $FLS2^{S938A}$ and $FLS2^{S938D}$ in cells after treatment with flg22 for different times as measured by FCS. (**E**) Immunoblot analysis of FLS2 protein in PM levels upon stimulation with or without flg22.

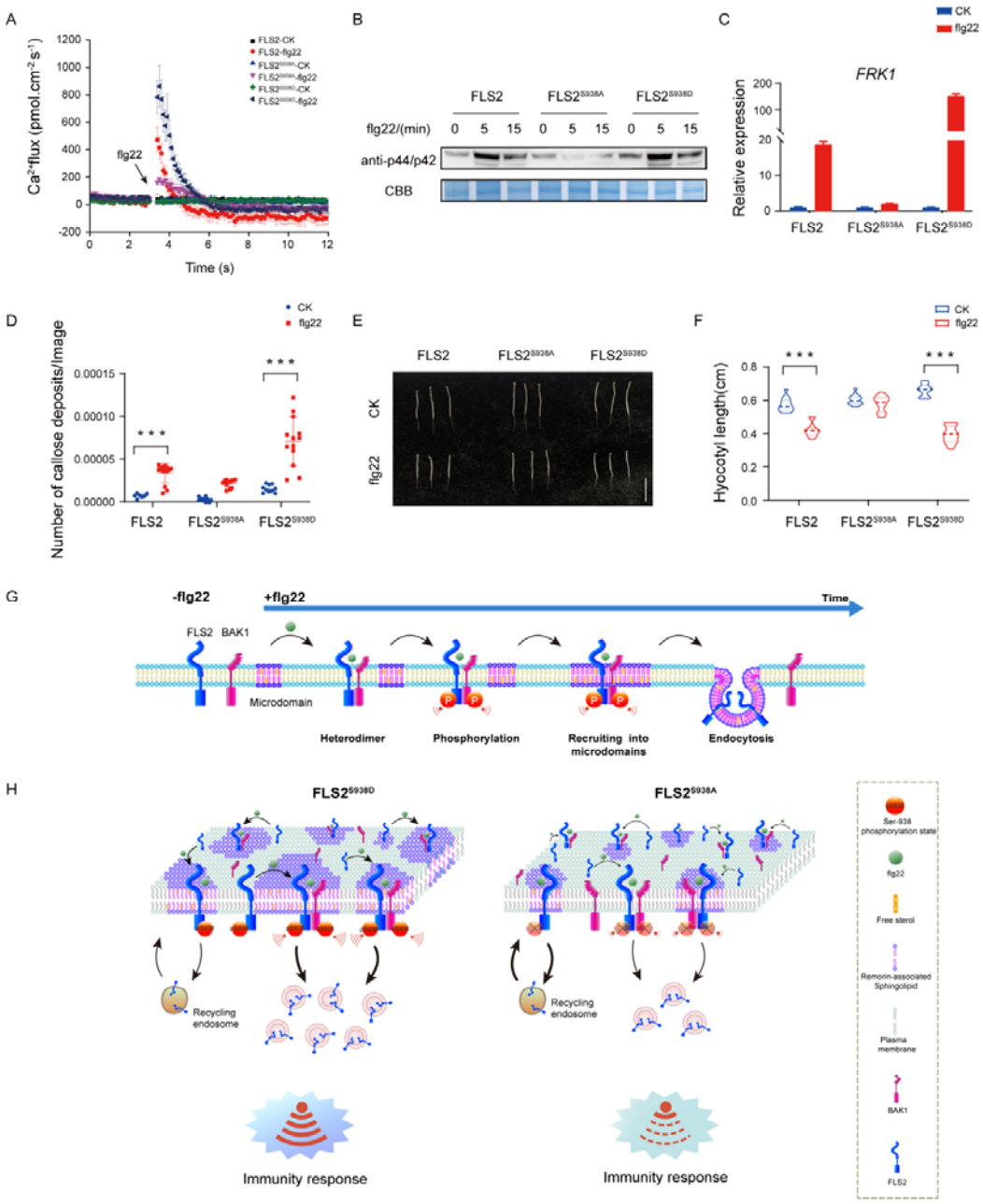

Figure 4. Ser-938 phosphorylation is essential for various flg22-induced PTI responses.

(**A**) The flg22-induced transient Ca^{2+} flux in leaf cells. The Ca^{2+} flux was continuously recorded in test medium for 12 min. (**B**) MAPKs phosphorylation in FLS2, $FLS2^{S938A}$, and $FLS2^{S938D}$ seedlings incubated with flg22 for 0min, 5min, and 15min. (**C**) mRNA levels of the PTI marker genes FRK1 were significantly different between FLS2, $FLS2^{S938A}$ and $FLS2^{S938D}$ *Arabidopsis*

after treatment with 10 μM flg22 for 30 min. (**D**) Phenotypes of 5-day old etiolated seedlings grown in the presence of 1/2 MS (CK) or 10 μM flg22 solid medium. Scale bar=0.5cm. (**E**) Hypocotyl length of FLS2, $FLS2^{S938A}$ and $FLS2^{S938D}$ plants. (**F**) The amount of callose stained with aniline blue per unit area on each image was quantitatively analyzed. (**G**) Working model for the spatiotemporal dynamic regulation of FLS2 phosphorylation at the plasma membrane upon stimulation with flg22. (**H**) Dynamic model of FLS2 with different Ser-938 phosphorylation states upon stimulation with flg22.